Journal of Energy Storage 106 (2025) 114742

Contents lists available at ScienceDirect

Journal of Energy Storage

journal homepage: www.elsevier.com/locate/est

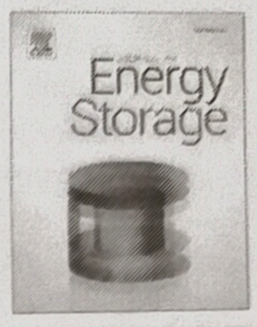

Research papers

One-step preparation of waste epoxy resin-derived nanosized carbon aerogel and its high supercapacitor performance

Chongjun Zhao *, Haimin Ou, Chunhua Zhao

Key Laboratory for Ultrafine Materials of Ministry of Education, Shanghai Key Laboratory of Advanced Polymeric Materials, School of Materials Science and Engineering, East China University of Science and Technology, Shanghai 200237, PR China

ARTICLE INFO

Keywords:
Carbon aerogel
Waste epoxy resin
Block
One-step preparation
Supercapacitor

ABSTRACT

Energy storage devices serve critical roles in both harvesting energy from new energy sources and supplying energy to consumers, and the performance of supercapacitors is heavily reliant on the performance of activated material, which is determined by the qualities achieved during the specified preparation process. Herein, due to the merit of isotropy of 0D carbon nanoparticles in structure and current transfer, spherical carbon aerogels (CA) with the size of $\phi \sim 100$ nm are carbonized within 3 min in air in an open tube furnace, in which those waste epoxy resin blocks are chosen and reused as the carbon source. After the activation, the surface of activated CA (ACA) becomes rough, and its specific surface area reaches 1222.40 $m^2 \cdot g^{-1}$. The above ACA owns high electrochemical supercapacitor performance: Referring to the ACA-based electrode, a specific capacitance of 298.8 $F \cdot g^{-1}$ at 1 $A \cdot g^{-1}$ and 92.81 % retention after 20,000 cycles of repeated charge/discharge. As for its symmetric supercapacitor (SSC), it has good CV behavior even at 1000 $mV \cdot s^{-1}$, accompanied by an energy density of 20.92 W h·kg $^{-1}$ at the power density of 300 W·kg $^{-1}$, and 12.34 W h·kg $^{-1}$ even at 12000 W·kg $^{-1}$.

1. Introduction

Due to pollution and the impending depletion of fossil fuels, it has become the secondary choice in energy sources. Clean and renewable power sources, such as sun, wind, and tidal, are now the top contenders. However, energy storage is required to receive and store the generated electricity [1,2]. Although both the battery (e.g., Li-ion battery, Li-S battery, and Zn-air battery) [3] and supercapacitor (SC) can be used to store the above electric energy, supercapacitor is widely employed in electric vehicles, aircraft, and power storage due to their merits, including high power density, outstanding cycling stability, and extended lifespan [4–7], but their energy density has still to be improved [8–9]. Currently, supercapacitors are classified as electric double-layer capacitors (EDLCs), pseudo-capacitors, and hybrid capacitors based on their storage mechanism [10]. Carbon-based supercapacitors, the most common type of electric double-layer capacitors, are popular in the commercial sector due to their excellent electrochemical stability, high power density, good electrical conductivity, long cycle life, and non-toxicity [11–13].

Up to now, one-dimensional (1D) nanosized carbon, including carbon nanotubes (CNT) [14], nanofibers [15], and nanorods [16], have been widely used in supercapacitor. Moreover, two-dimensional (2D) nanosized carbon containing graphene (including graphene oxide and reduced graphene oxide) [17,18] and nanosheets (curled) [19] are also exploited in the same field. However, the differences in current transfer and stress along various directions should be carefully considered, especially in the cases of the high power density (high current) and thick electrode due to the anisotropy of 1D and 2D (especially at curled state). Hence, the isotropy particles with a sphere or sphere-like shape may minimize the difference in current transfer and mechanic stress of the thick electrode, which facilitates its electrochemical performance and stability.

Due to its wide application as adhesives in composites and paint [20], the used epoxy resin waste has great potential in providing a rich carbon source. However, up to now, only a few works on epoxy resin-derived carbon as electrode materials are reported [21,22], and no nanosized carbon is prepared by using virgin or waste epoxy resin.

Besides, carbon aerogel is an ideal supercapacitor electrode material due to its high specific surface area, good chemical stability, and excellent electrical conductivity [23–28]. Now, carbon aerogel is usually prepared by typical Pekala's method, in which resorcinol and formaldehyde are chosen as the precursors [29]. Moreover, in a multi-step, at

* Corresponding author.
E-mail address: chongjunzhao@ecust.edu.cn (C. Zhao).

https://doi.org/10.1016/j.est.2024.114742
Received 24 July 2024; Received in revised form 18 October 2024; Accepted 20 November 2024
Available online 30 November 2024

least five steps are included: (i) Solation, (ii) Gelation (cured at 25–90 °C for several days to form a gel and aged at room temperature for several days to reinforce the gel), (iii) Solvent Exchange (a few hours or even a day), (iv) Drying, and (v) Carbonization (600–1200 °C for several hours). Furthermore, the preparation of nanosized aerogel carbon is dependent on the nanosized template of gel, i.e., no nanosized carbon aerogel is acquired if not nanosized but block precursor is supplied. The laborious, time-consuming, and expensive approach limits its use in supercapacitors [30,31]. Obviously, simplification of the preparation method and cost reduction are critical to promoting the use of carbon aerogels in supercapacitors.

Here, nanosized carbon aerogel is produced in 3 min using the bulk precursor of a waste epoxy resin block, with no template needed. Symmetric supercapacitors (SSC) with activated carbon aerogel electrodes exhibit a high energy density of 20.92 W h·kg^{-1} and a power density of 300 W·kg^{-1}, making them acceptable for practical applications. This work provides a new technique for efficiently preparing nanosized carbon aerogel and reuse of discarded epoxy resin in the future.

2. Experimental

2.1. Materials and reagents

The waste epoxy resin (Shanghai King Chemical Co. Ltd.) was cut to a size of 1 × 2 × 0.3 cm^3. Nickel foam, acetone (>98.5 %), ethanol (≥99.7 %), potassium carbonate (≥99.0 %), and potassium hydroxide (≥85.0 %) were bought from Shanghai Aladdin Biochemical Technology Company. Hydrochloric acid was obtained from Sinopharm Chemical Reagent. All chemicals were used without further purification.

2.2. Preparation of carbon aerogel

The waste epoxy resin was directly carbonized in air in an open tube furnace for 3 min to prepare the carbon aerogel. When the set temperature was reached, the epoxy resin was placed in a quartz tube. Subsequently, the gasified and solidified product was collected at the end of the downstream of the quartz tube. The obtained carbon aerogel samples were cleaned with acetone, alcohol and deionized water and then dried at 80 °C, which were named CA-T (T is carbonization temperature, and T = 500, 600, 700, 800, 900, 1000, and 1100 °C). For comparison, carbon samples from the residue of epoxy resin suffered from the carbonization process at 900 °C in N_2 for 3 min or 3 h, which were termed NC-900-3M and NC-900-3H, respectively.

2.3. Chemical activation of carbon

CA-900 was further activated at 650 °C in N_2 atmosphere for 180 min with different doses of solid KOH and K_2CO_3 additions (5:0, 6:0, 7:0, 5:1, and 4:2). ACA was named ACA-X-Y (X = 4, 5, 6, and 7; Y = 0, 1, and 2), in which X and Y refer to the mass ratio of KOH and K_2CO_3, respectively. For comparison, NC-900-3M and NC-900-3H were activated at the same condition with the mass ratio of NC: KOH: K_2CO_3 = 1:5:1, which were named ANC-900-3M and ANC-900-3H. All the activated CA (ACA) and activated NC (ANC) samples were cleaned with diluted hydrochloric acid and deionized water and then dried at 80 °C for 6 h.

2.4. Characterization of activated carbon aerogel (ACA)

A field emission scanning electron microscope (FESEM, Hitachi, S-4800) was used to observe the morphology and the size of activated carbon aerogel. For the investigation of the BET surface area and the porosity, Micromeritics ASAP 2460 was adopted. Fourier transform infrared spectroscopy (FTIR, Nicolet 6700) was used to analyze the surface chemical functional groups of the samples, while Raman spectroscopy (Invia reflex, Renishaw Instruments, England) was utilized to learn the chemical changes in carbon material at room temperature. The elements and chemical state analysis of the samples was evaluated by X-ray photoelectron spectroscopy (XPS, ESCALAB 250 Xi), and all XPS peaks were calibrated with the C 1s line at 284.8 eV.

2.5. Electrochemical measurements of activated carbon aerogel

Powdery ACA clamped by two nickel foams with a work area of 1 × 1 cm^2, acted as the working electrodes. Hg/HgO and Pt foil were used as the reference electrode and the counter electrode, respectively. The electrochemical measurements were run in an aqueous solution of 6.0 M KOH on the electrochemical workstation (CHI660E, Shanghai Chenhua). Referring to the three-electrode system, the potential window was −1–0 V, and the cyclic voltammetry (CV) measurement was performed at scan rates from 5 to 500 mV·s^{-1}, while the galvanotactic charge and discharge (GCD) at current densities from 0.5 to 30 A·g^{-1}. As for the two-electrode system, the voltage window was 0–1.2 V, and the CV curves were displayed at scan rates from 5 to 1000 mV·s^{-1}, while GCD curves at current densities from 0.5 to 20 A·g^{-1}. The frequency range of electrochemical impedance spectroscopy (EIS) was 10^5–0.01 Hz with a disturbance of 5 mV.

Based on the charge/discharge time of the measured GCD curves of the electrode materials, the specific capacitance (Cs, F·g^{-1}) of both the three-electrode system and SSC, the energy density (E, W h·kg^{-1}) and the power density (P, W·kg^{-1}) of SSC are calculated with the following equations:

$$Cs = \frac{I^*\Delta t}{m^*\Delta V} \quad (1)$$

$$E = \frac{Cs^*\Delta V^2}{2^*3.6} \quad (2)$$

$$P = \frac{E}{\Delta t}{}^*3600 \quad (3)$$

where I (A) is the charge/discharge current, Δt (s) is the discharge time, m (g) is the mass of the working electrode, and ΔV (V) is the selected voltage window.

3. Results and discussion

3.1. Preparation of carbon aerogel from epoxy resins

High temperatures are typically associated with phenomena such as pyrolysis, evaporation, and carbonization. As a result, the treatment temperatures have a significant impact on carbon aerogel synthesis. After being treated at high temperatures, the results consist of three components: residual carbon, waste gas [32], and carbon aerogel. Obviously, the carbon aerogel and waste gas grow with temperature, while the leftover carbon decreases.

Scheme 1 configures the whole preparation process of CA and NC. The generated carbon aerogel can be disregarded at 500 °C, and the epoxy resin primarily transforms into carbon blocks. When the temperature rises, the resin-derived carbon starts to lessen and is fully eliminated at 800 °C. Conversely, the amount of the obtained carbon aerogel increases with temperature up to 900 °C, after which it barely changes, even at 1100 °C. Regarding the carbon aerogel preparation period, 3 min is selected since after treating the epoxy resin in the furnace for >3 min at 900 °C, no residue is seen. Moreover, the bulk density of CA-900 is 0.06 g·cm^{-3}. In comparison, in N_2 atmosphere, no carbon aerogel but carbon block is generated even when the epoxy resin is suffering from the same temperature of 900 °C in 3 min or even over 3 h, as shown in Fig. S1. The optimal conditions for preparing carbon aerogel from waste epoxy resins include a temperature of 900 °C and a duration of 3 min, as well as abundant oxygen in the air.

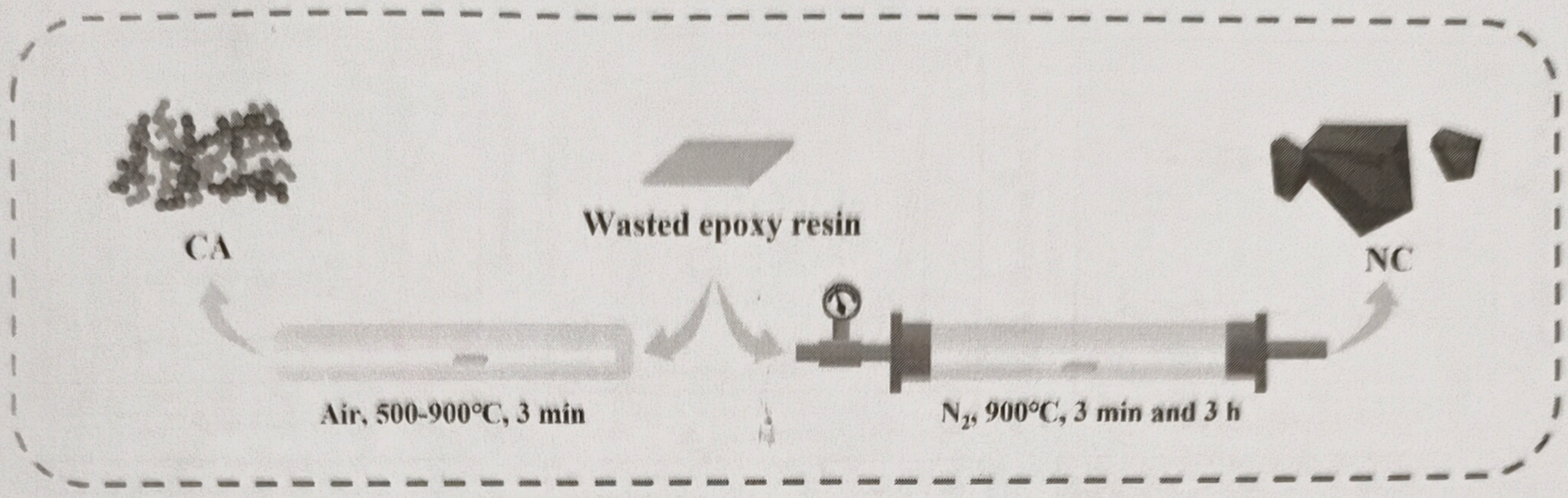

Scheme 1. Schematic for preparation of carbon aerogel (CA) and carbonized in N_2 (NC).

3.2. Morphological structure and chemical state

As shown in the SEM images of CA-900 in Fig. 1a and b, despite the bulk precursor of a waste epoxy resin block of 1 × 2 × 0.3 cm^3, a nanosized carbon aerogel sphere with an average diameter of 100 nm is directly prepared through a one-step process without any template. Moreover, upon the activation process, the smooth surface of carbon aerogel nanoparticles becomes rough (Figs. S2 and 1a–f), which improves the specific surface area and active sites of the carbon aerogels [33] and thus facilitates their electrochemical performances, which are later discussed. It is worth noting that the mixture active agent of KOH and K_2CO_3 endows a better uniform surface to carbon aerogels than the single active agent of KOH (Fig. 1c–f), which is consistent with the previously reported work [34].

The improvement on the specific surface area (SSA) and pore distribution are further confirmed by the nitrogen adsorption-desorption test. As shown in Fig. 2a, the adsorption-desorption isotherms of all samples belong to the category I isotherms, according to the classification of the International Union of Pure and Applied Chemistry (IUPAC) [35]. In addition, the specific performance is an obvious and rapid adsorption trend at low relative pressure ($P/P_0 < 0.1$), which suggests the existence of the abundant micropores, and the isotherm has a sloping and clear hysteresis loop in the region of $P/P_0 > 0.4$, indicating the existence of small-sized mesopores in the structure [36]. The porosity parameters of the samples are listed in Table 1. The BET specific surface areas of ACA-6-0 and ACA-5-1 are 1208.59 and 1222.40 $m^2 \cdot g^{-1}$, respectively, and the ACA samples have a good pore volume and micropore volume, which favors the formation of a three-dimensional (3D) porous interconnection network [37]. Furthermore, as given in Fig. 2b and Table 1, ACA-6-0 possesses mesopore size around 5–10 nm, while the ACA-5-1 is 2–5 nm. As listed in Table 1, the pore volumes of ACA-6-0 and ACA-5-1 are 0.70 and 0.67 $cm^3 \cdot g^{-1}$, and their micropore volumes reach 0.26 and 0.37 $cm^3 \cdot g^{-1}$, respectively.

Fig. 2c presents the FTIR spectra of CA-900 and ACA samples, displaying the vibration of different functional groups on the surface of carbon aerogel. 3423 cm^{-1} shows a broad, strong characteristic absorption peak, which corresponds to the stretching hydroxyl vibration (O-H) of carboxylic acids [38]. On the other hand, as shown in Fig. 2c, upon activation, -OH (1232 cm^{-1}) [33] and C-O-C (1094 cm^{-1}) [39] functional groups are greatly enhanced, which suggests that the affinity of the carbon surface to the electrolyte is improved and thus produces an additional specific capacitance [40,41]. Moreover, mixed activated agents of KOH and K_2CO_3 introduce more aromatic CO- and phenolic -OH in carbon aerogels than KOH activation, as shown in Fig. 2c.

Fig. 2d-f give the Raman spectra of CA-900, ACA-6-0, and ACA-5-1, in which two notable vibration bands (D-band at 1350 cm^{-1}, G-band at 1580 cm^{-1}) of hexagonal graphite are clearly observed [42]. D-band, defects in the carbon atom lattice, corresponds to the amorphous form, while G-band, the in-plane stretching vibration of sp^2 hybridization of carbon atoms, is assigned to the graphite state of the carbon aerogel

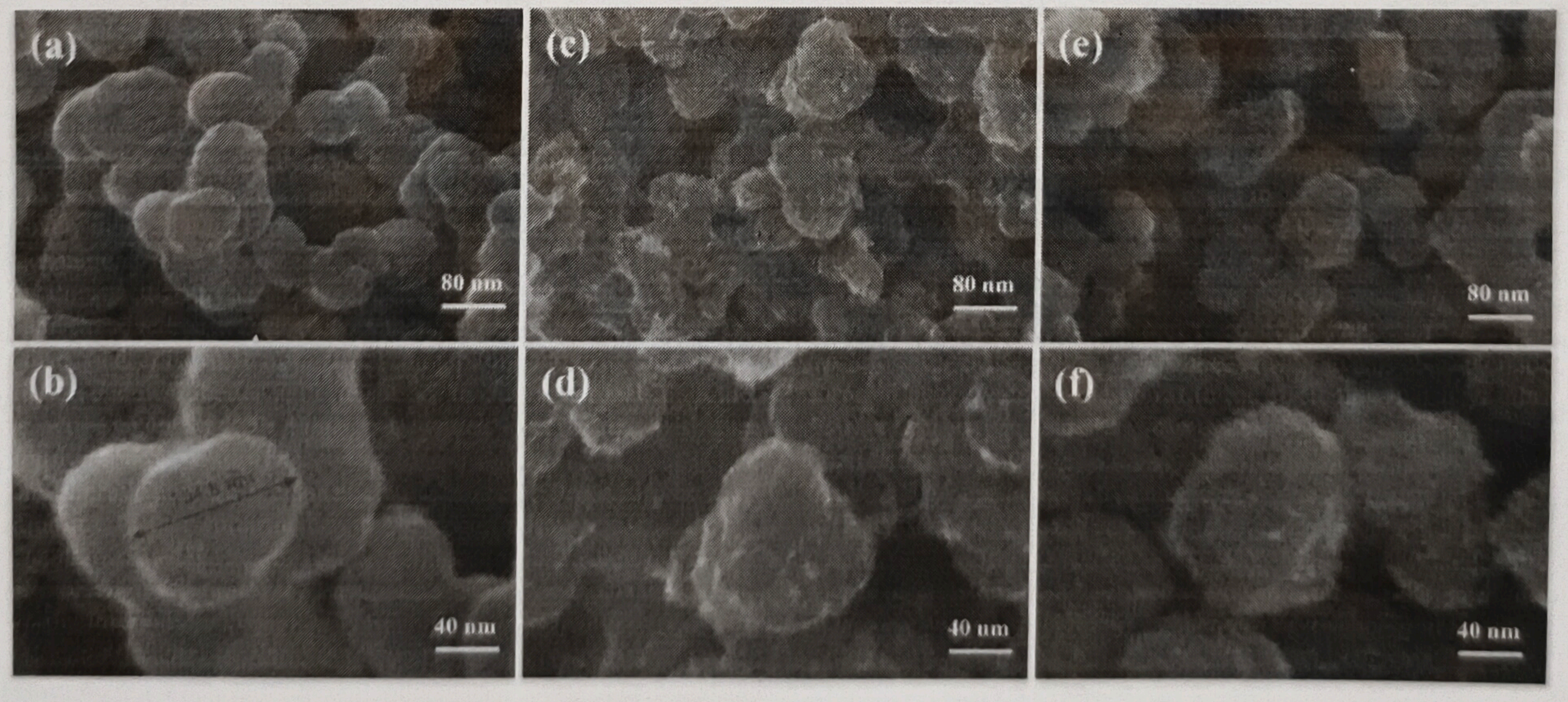

Fig. 1. SEM images of (a, b) CA-900, (c, d) ACA-6-0, and (e, f) ACA-5-1.

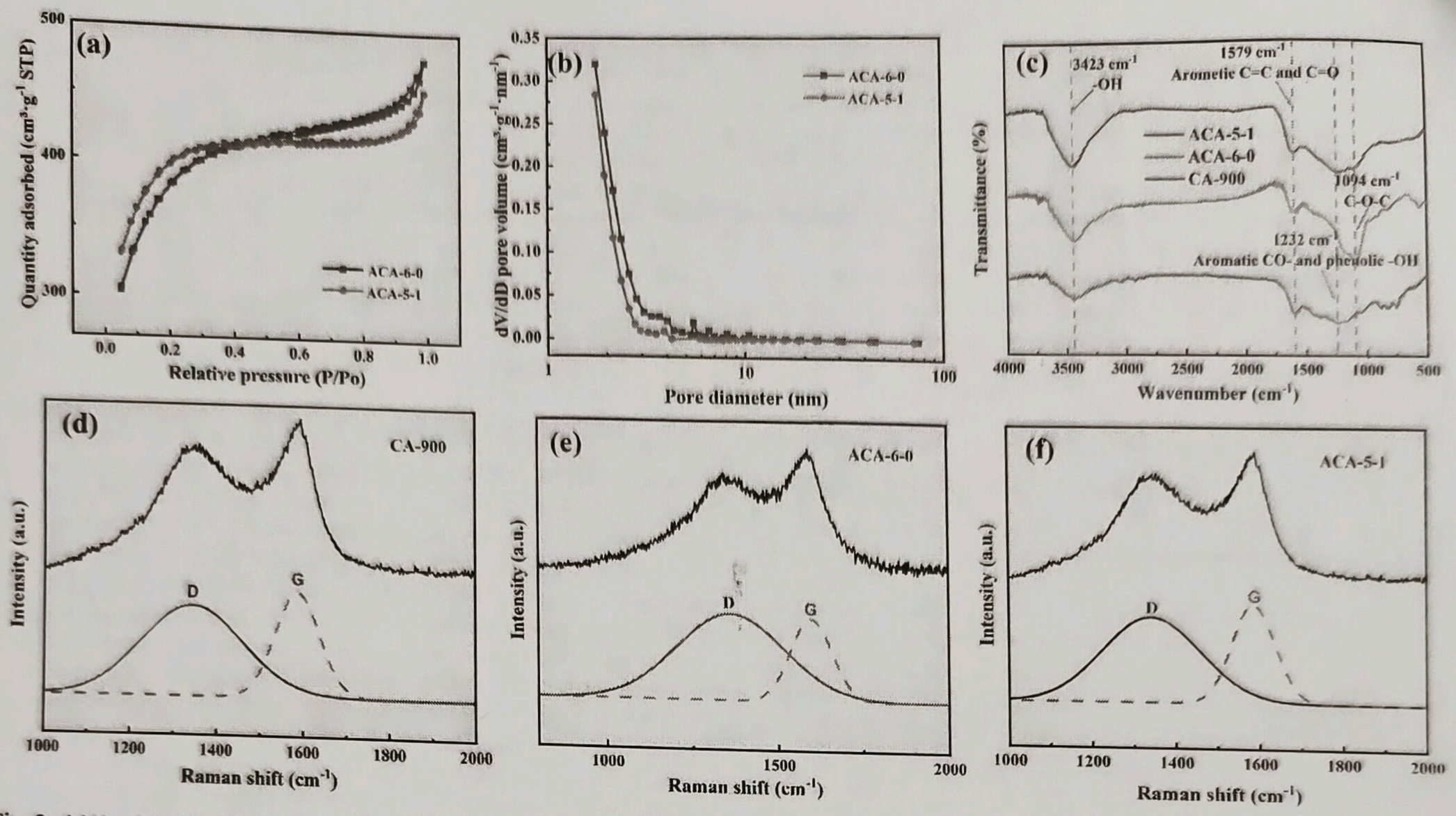

Fig. 2. (a) N_2 adsorption/desorption isotherms and (b) BJH pore size distribution curves of ACA-6-0 and ACA-5-1. (c) FTIR spectra and (d–f) Raman spectra of CA-900, ACA-6-0, and ACA-5-1.

Table 1
Porosity parameters of the ACA samples.

Sample	S_{BET} ($m^2 \cdot g^{-1}$)	Pore volume ($cm^3 \cdot g^{-1}$)	Micropore volume ($cm^3 \cdot g^{-1}$)	Average pore size (nm)
ACA-6-0	1208.59	0.70	0.26	2.32
ACA-5-1	1222.40	0.67	0.37	2.18

samples [42,43]. Hence, the ratio of D and G peaks (I_D/I_G) is used to determine the degree of amorphousness of the material, i.e., the degree of defects [44]. As listed in Table 2, I_D/I_G increases after activation, especially for mixed activated agent (ACA-5-1), suggesting more defects for ACA samples. These indicate that ACA samples have more pores or defects, which provide a higher surface area and active site species and thus improve the electrochemical performance [45].

Fig. 3 presents XPS of CA-900 before and after activation treatment, and the elemental contents are listed in Table 3, in which C content is majority, N is minority, and O is middle. Moreover, as presented in Fig. 3a, d, and g, chemical activation increases the oxygen contents and decreases the C contents and N contents, and the mixed active agent of KOH and K_2CO_3 is milder than KOH in introducing oxygen functional groups, which is consistent with the previous FTIR results. As given in the deconvolution of C 1s in Fig. 3b, e, and h, five functional groups, assigning to the sp^2 C=C (284.0 eV), sp^3 C-C (284.8 eV), C-O-C (286.0 eV), O-C=O (288.5 eV), and C=O (289.6 eV) are observed [46–48].

Table 2
Ratio of I_D/I_G of the CA-900 before and after chemical activation.

Sample	I_D/I_G
CA-900	0.86
ACA-6-0	0.91
ACA-5-1	1.05

Moreover, the O 1s deconvolution spectrum displays three staple peaks, assigned to C-OH (533.4 eV), C=O (532.5 eV), and quinone (531.2 eV), respectively [49]. In the C 1s spectra of ACA-6-0 and ACA-5-1, the content of C=O groups increases after activation, whereas in the O 1s spectra of ACA-5-1, the content of C=O groups decreases and quinone content increases after activation. This may be due to the layered structure of the carbon aerogel being destroyed when the carbon-carbon double bond in the hexagonal ring is extensively oxidized by solid KOH activation.

3.3. Electrochemical performances of the ACA-based electrode

The CA-900 activated with various alkali ratios was studied in order to determine the best activation scheme (Figs. S3 and S4). Firstly, as shown in Fig. S2, the surface of carbon aerogel nanoparticles becomes rough, which improves the surface area and thus the active sites. Secondly, as shown in Fig. S3, at the 5, 6, and 7 doses of single active agents of solid KOH, ACA obtained with 6 doses of solid KOH, ACA-6-0 exhibits the highest specific capacitance (198.2 vs. 195.9 and 180.6 $F \cdot g^{-1}$) and the best ratability. Thirdly, when the ratio of CA to total active agent is kept at 1:6, as shown in Fig. S4, ACA-5-1 (298.8 $F \cdot g^{-1}$) delivers the prior electrochemical performance (specific capacitance and ratability) to other ACA samples (i.e., 198.2 $F \cdot g^{-1}$ for ACA-6-0 and 228.1 $F \cdot g^{-1}$ for ACA-4-2). Hence, the optimal ratio of solid KOH and K_2CO_3 is 5:1. As shown in Figs. S3d and S4d, Nyquist curves in EIS consist of typical characterization of EDLC, i.e., semicircle at high frequency, vertical line at low frequency, and short slope line at middle frequency region. As the diameter of this semicircle determines the charge-transfer resistance (Rct), while the intercept at the real axis stands for the internal resistance (Rs), the values of Rct and Rs are calculated and listed in Table S1. Moreover, all these Rct and Rs data are $<1.0\ \Omega$, which are obviously less than those carbon aerogels derived from other carbon sources [50–53].

In order to verify the electrochemical performance of the epoxy resin-derived carbon aerogels, another two carbon samples from epoxy resins are prepared at 900 °C in N_2 atmosphere for 3 min and 3 h, i.e.,

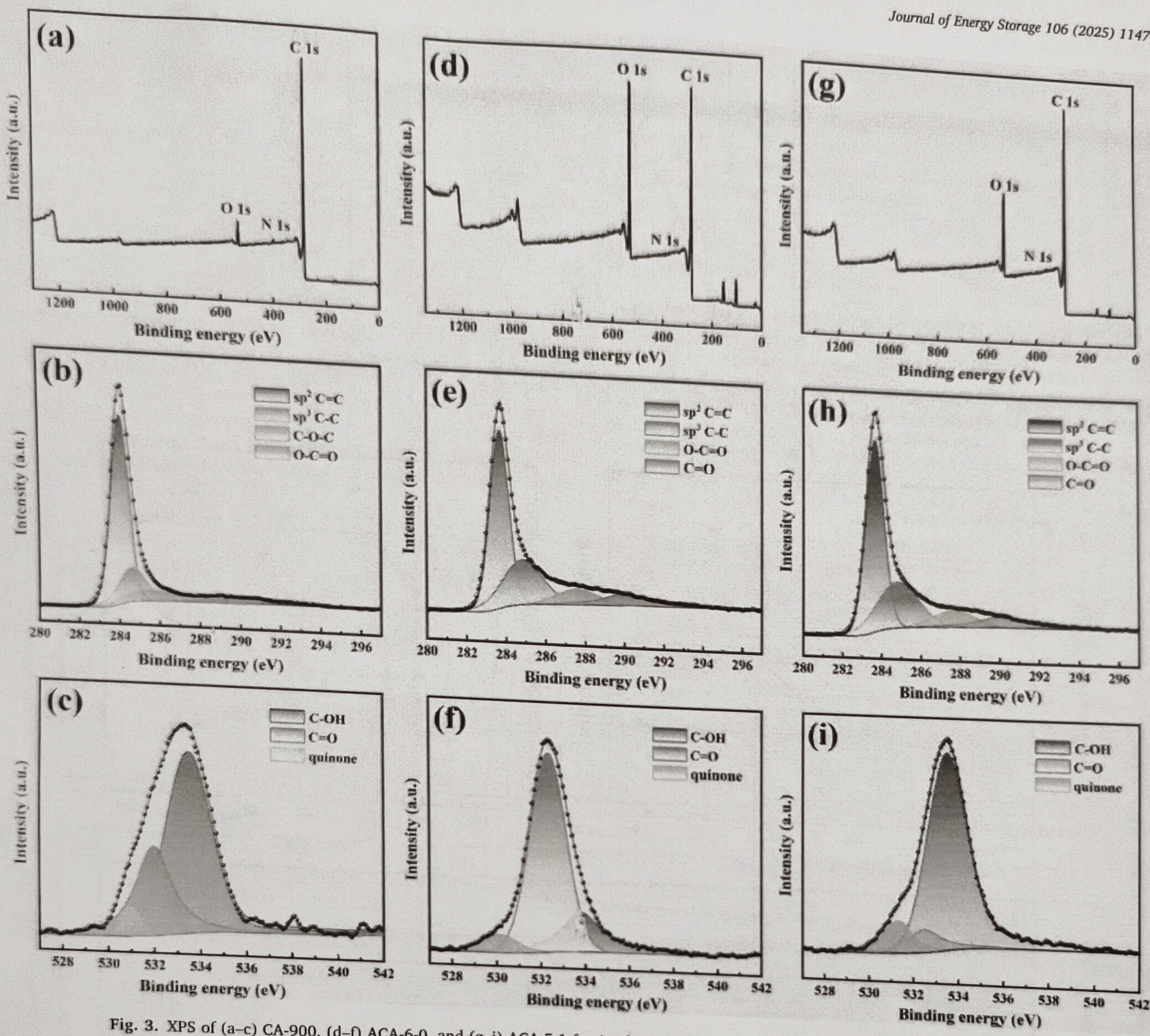

Fig. 3. XPS of (a–c) CA-900, (d–f) ACA-6-0, and (g–i) ACA-5-1 for (a, d, g) survey spectrum, (b, e, h) C 1s, and (c, f, i) O 1s spectra.

Table 3
Element analysis of the CA-900 before and after chemical activation (wt%).

Sample	C 1s	O 1s	N 1s
CA-900	92.41	5.89	1.71
ACA-6-0	71.96	26.60	1.44
ACA-5-1	83.95	15.16	0.88

ANC-900-3M and ANC-900-3H. As shown in Fig. 4a, the area of the CV curve for ACA-5-1 is significantly larger than others, and the specific capacitances of ACA-5-1, ANC-900-3H, and ANC-900-3M is 289.8, 148.3, and 56.0 $F \cdot g^{-1}$, respectively (Fig. 4b). As can be seen in Fig. 4c, the specific capacitance of ACA-5-1 tends to slowly decrease with increasing current density from 1 to 30 $A \cdot g^{-1}$, and the retention of specific capacitance for ACA-5-1, ANC-900-3H, and ANC-900-3M are 67.3 %, 14.2 %, and 16.1 %, respectively. Obviously, carbon aerogels prepared in air have significantly higher specific capacitance and ratability than epoxy resin-derived carbons prepared in N_2 atmosphere for 3 min or 3 h.

The high specific capacitance and ratability of ACA-5-1 may be attributed to its unique three-dimensional porous interconnection network, which facilitates the storage of ions in the electrolyte and provides low-resistance channels for ion transport [54,55]. Hence, aerobic carbonization in air is an efficient way to convert epoxy resin into active carbon with high performance.

Fig. 5a shows CV curves of ACA-5-1 at different scan rates, in which a quasi-rectangular shape is maintained even at a scan rate of 500 $mV \cdot s^{-1}$. Moreover, based on the GCD curves in Fig. 5b, the specific capacitance at 30 $A \cdot g^{-1}$ still reaches 201.0 $F \cdot g^{-1}$, which means 67.3 % retention at 1 $A \cdot g^{-1}$ (298.8 $F \cdot g^{-1}$) at a 30 times current density. Referring to the cycle stability, as present in the cycle test in Fig. 5c, 92.81 % retention of the initial specific capacitance is kept even after 20,000 times running, which maybe resulted from the stable structure of the electrode consisting of isotropy aerogel carbon sphere nanoparticles. Moreover, compared with those activated carbon aerogels derived from other carbon sources [56–60] (Table 4), the optimized carbon aerogel in our work, ACA-5-1, exhibits a comparable or prior electrochemical performance in 6 M KOH.

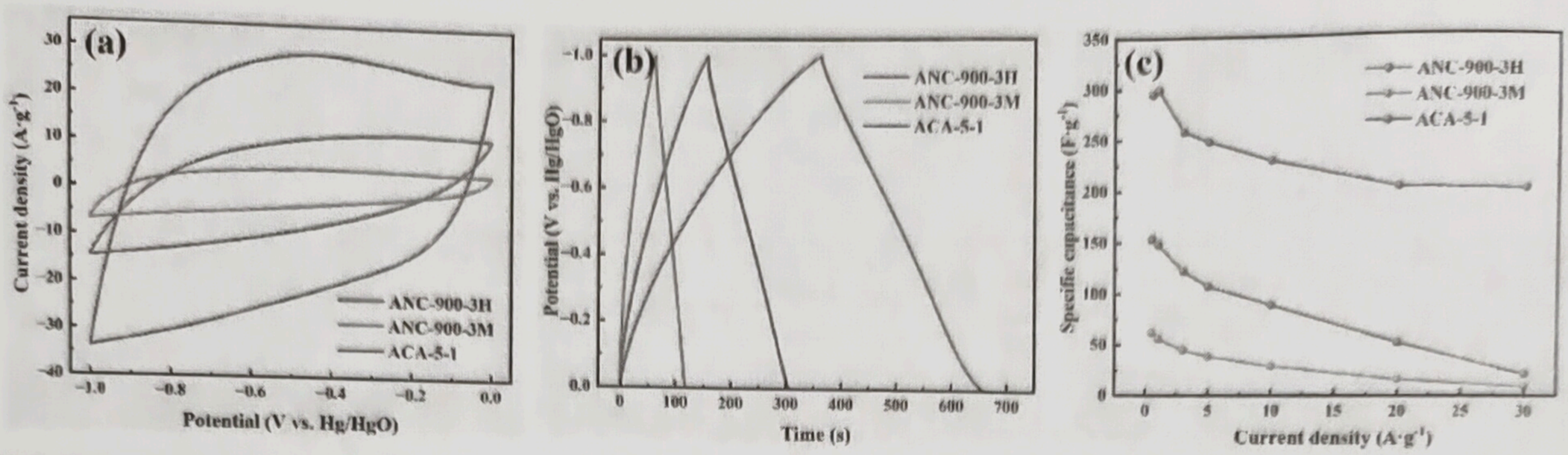

Fig. 4. Electrochemical performances of ANC-900-3H, ANC-900-3M, and ACA-5-1 in 6 M KOH in a three-electrode system: (a) CV curves at 100 mV·s $^{-1}$, (b) GCD curves at 1 A·g^{-1}, (c) ratability, and (d) Nyquist plots.

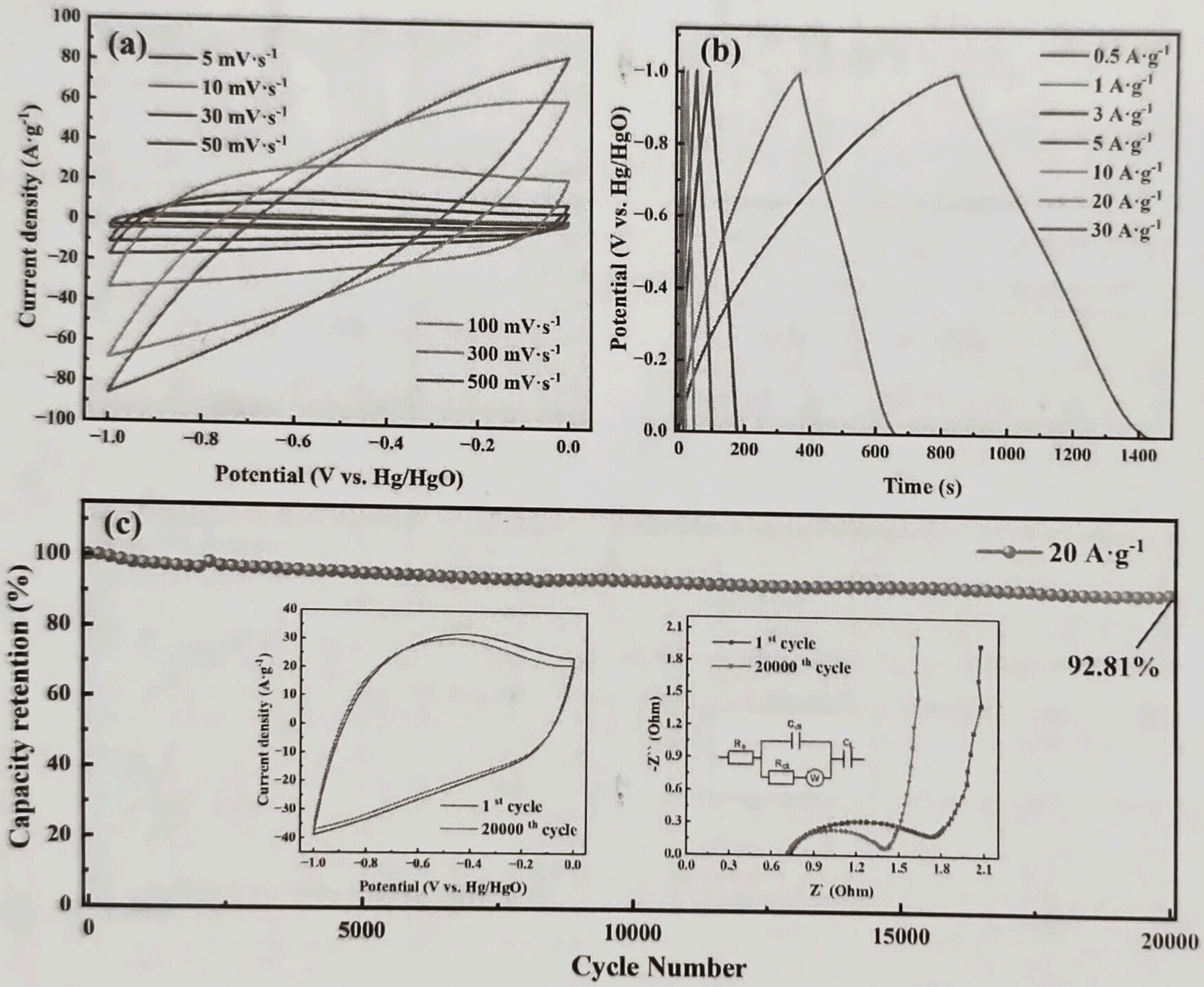

Fig. 5. Electrochemical performances of ACA-5-1 electrode in 6 M KOH in a three-electrode system: (a) CV curves at different scan rates from 5 to 500 mV·s $^{-1}$, (b) GCD curves at various current densities from 0.5 to 30 A·g^{-1}, (c) cyclic test at 20 A·g^{-1}, inset left: CV curves and inset right: EIS spectra of first and last cycles.

3.4. Electrochemical performances of symmetric supercapacitor

A symmetric supercapacitor (SSC) made of two electrodes based on ACA-5-1 that function as both the anode and the cathode is created in order to assess the practical applicability of ACA-5-1 even more. The CV curves in various voltage windows are displayed in Fig. 6a. When the voltage window of 1.3 V is selected, there is a clear polarization at the end of the voltage. As given in the energy density equation of Eq. (2). The square of the applied voltage determines the energy density. As a result, 1.2 V rather than 1.1 V is chosen as the SSC's work voltage. As shown in Fig. 6b, the envelopes of CV curves increase with the scan rates, and no obvious distortion occurs on the shape of the CV curve even when the scan rate reaches 1000 mV·s^{-1}, suggesting that this SSC of ACA-5-1//ACA-5-1 owns excellent ratability. Furthermore, based on the GCD curves (Fig. 6c), the specific capacitances at 0.5, 1, 2, 3, 5, 10, and 20 A·g^{-1} are calculated to be 104.6, 91.0, 84.0, 80.0, 75.8, 69.2, and

Table 4
Comparison o

Table 4
Comparison of the electrochemical performance of ACA-5-1 with those of the activated carbon aerogels from other carbon sources.

Carbon sources	Activator	Specific capacitance ($F \cdot g^{-1}$)	Refs
Starch	KOH	211.5 (0.5 $A \cdot g^{-1}$)	[56]
Plectocomia rattan	KOH	221.0 (0.5 $A \cdot g^{-1}$)	[57]
Resorcinol-Lignin	KOH	142.8 (0.5 $A \cdot g^{-1}$)	[58]
CMC	KOH	152.6 (0.5 $A \cdot g^{-1}$)	[59]
Sliced bread	KOH	229.0 (0.2 $A \cdot g^{-1}$)	[60]
Epoxy resin	KOH + K_2CO_3	298.8 (1.0 $A \cdot g^{-1}$)	This work

61.7 $F \cdot g^{-1}$, respectively. Consequently, the energy density and power density of SSC of ACA-5-1//ACA-5-1 are acquired: A considerable energy density of 20.92 W $h \cdot kg^{-1}$ at the power density of 300 W $\cdot kg^{-1}$ and 12.34 W $h \cdot kg^{-1}$ at 12000 W $\cdot kg^{-1}$. As given in the Ragone plot in Fig. 6d, the electrochemical performance of this SSC is superior to those previously reported devices, which use pure activated carbon as the electrode materials [61–66]. In addition, SSC of ACA-5-1//ACA-5-1 has a high cycle life, as shown in Fig. 6e, 80.12 % retention of the specific capacitance is still maintained after 10,000 repeated charge/discharge cycles. Lastly, as shown in Fig. S5, two SSC connected in series as a power supply can even drive three LEDs in parallel at the same time.

3.5. Storage mechanism of ACA-5-1

The charge storage mechanism of ACA-5-1 is further investigated by using the following computational model [67]:

$$i = av^b \tag{4}$$

$$logi = blogv + loga \tag{5}$$

where both *a* and *b* are determined by the intercept and slope of the fit line of *logi* as the function of *logv* in Eq. (5). b is usually used to provide kinetic information of the electrochemical behaviors, which varies in the range 0.5 to 1 [68]: the current is controlled by semi-infinite diffusion b = 0.5, while capacitive behavior b = 1. As b is 0.91 (Fig. 6f), the storage of ACA-5-1 is considered a capacitive behavior.

The capacitance contribution of the ACA-5-1 can be further distinguished based on Eqs. (6)–(7) [69].

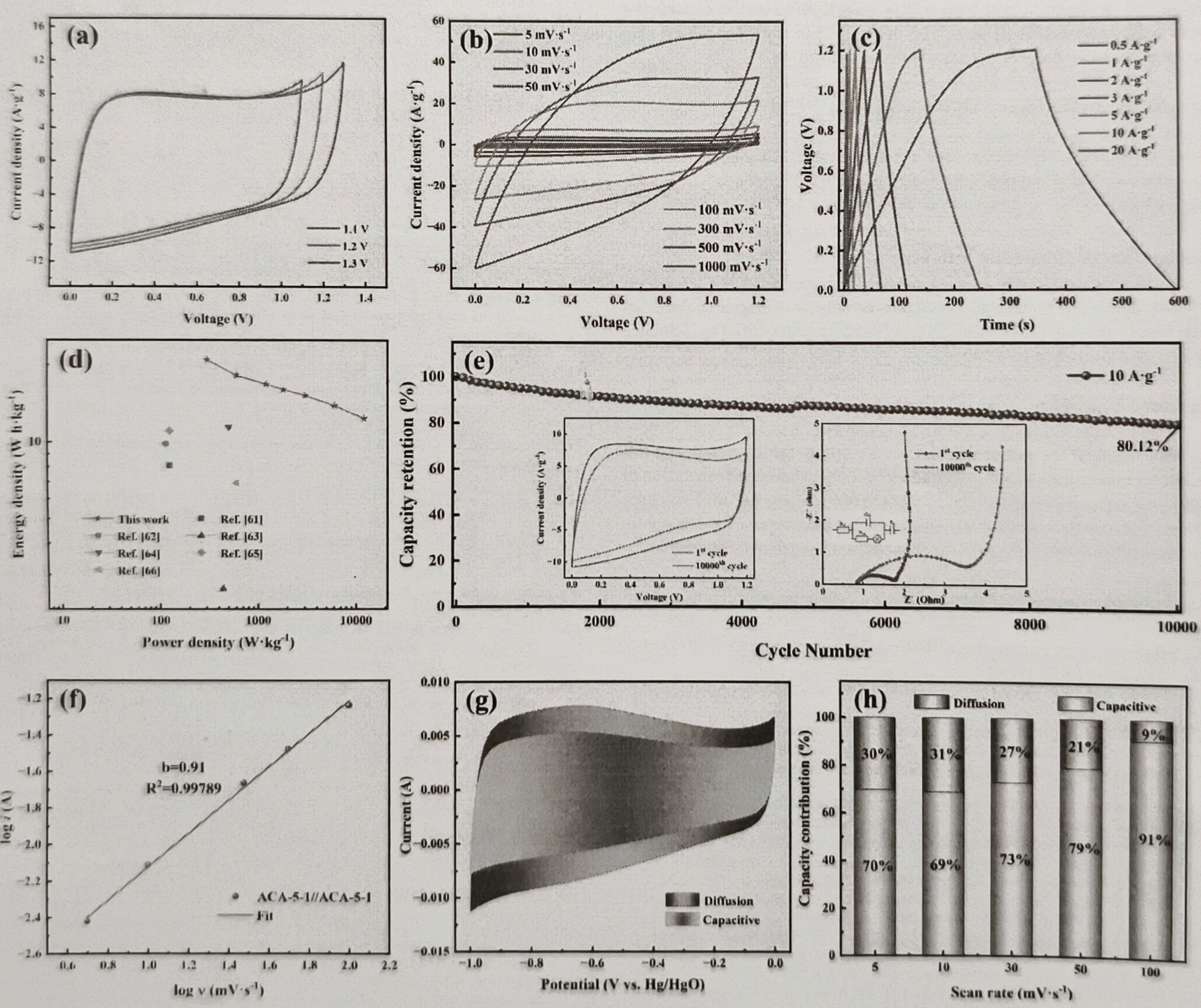

Fig. 6. Electrochemical performances of the SSC device of ACA-5-1//ACA-5-1: CV curves (a) in different voltage windows and (b) for a series of scan rates from 5 to 1000 mV $\cdot s^{-1}$, (c) GCD curves ranging from 0.5 to 20 A $\cdot g^{-1}$, (d) Ragone plots, and (e) cyclability. The results of computing: (f) linear fit plot of *logi* and *logv*. (g) Diffusion contribution and capacitive contribution in the CV curves at 10 mV $\cdot s^{-1}$. (h) Normalized capacitive contribution for a series scan rates from 5 to 100 mV $\cdot s^{-1}$.

$$i(V) = k_1 v + k_2 v^{1/2} \tag{6}$$

$$i(V)/v^{1/2} = k_1 v^{1/2} + k_2 \tag{7}$$

As shown in Fig. 6g and h, the capacitive contribution increases with the scan rates and reaches 91 % at 100 $mV{\cdot}s^{-1}$. These indicate that the dynamic process of ACA-5-1 is dominated by capacitance behavior.

4. Conclusions

Carbon aerogel with $\phi \sim 100$ nm is prepared by carbonizing waste epoxy resin within 3 min in air in an open tube furnace, in which oxygen and temperature play key roles. Activated carbon aerogel (ACA) at the optimum conditions has uniform porosity and a high specific surface area of 1222.40 $m^2{\cdot}g^{-1}$. Optimized ACA owns good electrochemical performance: referring to its electrode, a high specific capacitance of 298.8 $F{\cdot}g^{-1}$ (at 1 $A{\cdot}g^{-1}$) and 92.81 % retention of the initial specific capacitance after 20,000 cycles. As for its SSC, good CV behavior even at 1000 $mV{\cdot}s^{-1}$ and an energy density of 20.92 W $h{\cdot}kg^{-1}$ at a power density of 300 $W{\cdot}kg^{-1}$ and 12.34 W $h{\cdot}kg^{-1}$ at 12000 $W{\cdot}kg^{-1}$. According to the result of computing, the storage of ACA-5-1 is considered a capacitive behavior, and the capacitive contribution increases with the scan rates and reaches 91 % at 100 $mV{\cdot}s^{-1}$. This work supplies a new strategy to reuse the waste epoxy resin in the future.

CRediT authorship contribution statement

Chongjun Zhao: Writing – review & editing, Methodology. **Haimin Ou:** Writing – original draft, Investigation, Formal analysis, Data curation. **Chunhua Zhao:** Supervision, Funding acquisition.

Declaration of competing interest

The authors declare that they have no known competing financial interests or personal relationships that could have appeared to influence the work reported in this paper.

Acknowledgements

The authors are grateful for the support of the National Natural Science Foundation of China (22075082). Natural Science Foundation of Shanghai (Nos. 19ZR1413000, 13ZR1411900), Shanghai Alliance Plan (Nos. LM201881, LM201751), Shanghai Leading Academic Discipline Project (B502), and Shanghai Key Laboratory Project (08DZ2230500).

Appendix A. Supplementary data

Supplementary data to this article can be found online at https://doi.org/10.1016/j.est.2024.114742.

Data availability

Data will be made available on request.

References

[1] X. Han, H. Sun, C. Xu, J. Zhu, H. Chen, High-performance asymmetric supercapacitors assembled with novel disc-like $MnCo_2O_4$ microstructures as advanced cathode material, J. Colloid Interface Sci. 667 (2024) 350–361, https://doi.org/10.1016/j.jcis.2024.04.087.

[2] J. Sun, C. Xu, H. Chen, A review on the synthesis of $CuCo_2O_4$-based electrode materials and their applications in supercapacitors, J. Materiomics 7 (2021) 98–126, https://doi.org/10.1016/j.jmat.2020.07.013.

[3] A. Feng, X. Zhu, Y. Chen, P. Liu, F. Han, Y. Zu, X. Li, P. Bi, Functional biomass-derived materials for the development of sustainable batteries, J. Electroanal. Chem. 11 (2024) e202400086, https://doi.org/10.1002/celc.202400086.

[4] Z. Guo, X. Han, C. Zhang, S. He, K. Liu, J. Hu, W. Yang, S. Jian, S. Jiang, G. Duan, Activation of biomass-derived porous carbon for supercapacitors: a review, Chin. Chem. Lett. 35 (2024) 109007, https://doi.org/10.1016/j.cclet.2023.109007.

[5] T. Zahra, A. Gassoumi, S. Gouadria, M. Abdullah, F.F. Alharbi, S. Aman, H.M. T. Farid, Facile fabrication of $BiFeO_3$/g-C_3N_4 nanohybrid as efficient electrode materials for supercapacitor application, Diam. Relat. Mater. 144 (2024) 110927, https://doi.org/10.1016/j.diamond.2024.110927.

[6] X. Ren, E. Bao, X. Liu, Y. Xiang, C. Xu, H. Chen, Advanced hybrid supercapacitors assembled with beta-$Co(OH)_2$ microflowers and microclews as high-performance cathode materials, Colloids Surf. A Physicochem. Eng. Asp. 667 (2023) 131391, https://doi.org/10.1016/j.colsurfa.2023.131391.

[7] J. Sun, X. Tian, C. Xu, H. Chen, Porous $CuCo_2O_4$ microtubes as a promising battery-type electrode material for high-performance hybrid supercapacitors, J. Materiomics 7 (2021) 1358–1368, https://doi.org/10.1016/j.jmat.2021.03.011.

[8] H. Chen, E. Bao, H. Sun, X. Ren, X. Han, Y. Wang, Z. Zhang, C. Luo, C. Xu, Sonochemical synthesis of CoNi layered double hydroxide as a cathode material for assembling high performance hybrid supercapacitor, J. Colloid Interface Sci. 664 (2024) 117–127, https://doi.org/10.1016/j.jcis.2024.03.083.

[9] A. Yasmeen, A.M. Afzal, M.W. Iqbal, A. Zaka, H.U. Hassan, T. Abbas, M. Usman, L. Wang, Y.M. Alanazi, S. Mumtaz, Enhanced the stability and storage capability of sulfide-based material with the incorporation of carbon nanotube for high-performance supercapattery device, J. Electrochem. Energy Convers. Storage 21 (2024) 021002, https://doi.org/10.1115/1.4062642.

[10] E. Bao, X. Ren, R. Wu, X. Liu, H. Chen, Y. Li, C. Xu, Porous $MgCo_2O_4$ nanoflakes serve as electrode materials for hybrid supercapacitors with excellent performance, J. Colloid Interface Sci. 625 (2022) 925–935, https://doi.org/10.1016/j.jcis.2022.06.098.

[11] Y.A. Kumar, J.K. Alagarasan, T. Ramachandran, M. Rezeq, M.A. Bajaber, A. A. Alalwiat, M. Moniruzzaman, M. Lee, The landscape of energy storage: insights into carbon electrode materials and future directions, J. Energy Storage 86 (2024) 111119, https://doi.org/10.1016/j.est.2024.111119.

[12] W. Fan, F. Wang, X. Xiong, B. Song, T. Wang, X. Cheng, Z. Zhu, J. He, Y. Liu, Y. Wu, Recent advances in functional materials and devices for Zn-ion hybrid supercapacitors, NPG Asia Mater. 16 (2024) 1–20, https://doi.org/10.1038/s41427-024-00537-9.

[13] Z. Zhai, L. Zhang, T. Du, B. Ren, Y. Xu, S. Wang, J. Miao, Z. Liu, A review of carbon materials for supercapacitors, Mater. Des. 221 (2022) 111017, https://doi.org/10.1016/j.matdes.2022.111017.

[14] S. Zhu, X. Yang, Y. Yao, X. Zhang, L. Li, X. Wang, G. Han, Y. Li, One-dimensional heterostructures of polyoxometalate-encapsulated carbon nanotubes for enhanced capacitive energy storage, Cell Rep. Phys. Sci. 4 (2023) 101446, https://doi.org/10.1016/j.xcrp.2023.101446.

[15] K. Rajendran, K. Lolupiman, M. Okhawilai, H.A. Therese, S. Kheawhom, P. Tan, J. Qin, Synthesis, formation mechanism and supercapacitor performance of MoS_2/Mo_2C/C nanofibers, J. Alloys Compd. 980 (2024) 173549, https://doi.org/10.1016/j.jallcom.2024.173549.

[16] X. Wang, F. Zhou, R. Jing, S. Gu, Q. Zhang, Z. Li, Y. Zhu, Z. Xiao, L. Wang, The precise building units modulation of iron-bismuth sulfide triple-level hierarchical structure for enhanced supercapacitor performance, J. Power Sources 597 (2024) 234128, https://doi.org/10.1016/j.jpowsour.2024.234128.

[17] F. Yao, W. Li, S.K. Sks, C. Fukuhara, S. Badhulika, C.Y. Kong, Scalable one-step synthesis of reduced graphene oxide: towards flexible transparent conductive films and active supercapacitor electrodes, Chem. Eng. J. 488 (2024) 150828, https://doi.org/10.1016/j.cej.2024.150828.

[18] M. Gautam, S. Kanade, B.B. Kale, Electrochemical energy storage and conversion applica- tions of graphene oxide: a review, Energy Fuel 37 (2023) 17134–17160, https://doi.org/10.1021/acs.energyfuels.3c02933.

[19] L.-J. Sun, X.-Y. Zhang, C. Bai, H.-L. Guo, C.-M. Han, Y.-F. Zhang, H.-M. Hu, Cobalt/nickel 2D MOF nanosheets with a bithiophene-tetraterpyridyl derivative ligand for high-performance supercapacitors through boosting pseudocapacitance, J. Energy Storage 92 (2024) 112197, https://doi.org/10.1016/j.est.2024.112197.

[20] Y. Zhang, X. Liu, M. Wan, Y. Zhu, K. Zhang, Recent development of functional bio-based epoxy resins, Molecules 29 (2024) 4428, https://doi.org/10.3390/molecules29184428.

[21] C. Zhao, S. Chen, N. Sun, W. Jiang, W. Cai, C. Zhao, Bisphenol A epoxy resin-derived activated carbon with high performance for supercapacitors, J. Phys. Chem. C 127 (2023) 18821–18831, https://doi.org/10.1021/acs.jpcc.3c03756.

[22] Y. Liu, J.S. Xue, T. Zheng, J.R. Dahn, Mechanism of lithium insertion in hard carbons prepared by pyrolysis of epoxy resins, Carbon 34 (1996) 193–200, https://doi.org/10.1016/0008-6223(96)00177-7.

[23] C. Xiong, Y. Zhang, Y. Ni, Recent progress on development of electrolyte and aerogel electrodes applied in supercapacitors, J. Power Sources 560 (2023) 232698, https://doi.org/10.1016/j.jpowsour.2023.232698.

[24] H. Liu, T. Xu, Q. Liang, Q. Zhao, D. Zhao, C. Si, Compressible cellulose nanofibrils/reduced graphene oxide composite carbon aerogel for solid-state supercapacitor, Adv. Compos. Hybrid Mater. 5 (2022) 1168–1179, https://doi.org/10.1007/s42114-022-00427-0.

[25] J. Mao, J. Iocozzia, J. Huang, K. Meng, Y. Lai, Z. Lin, Graphene aerogels for efficient energy storage and conversion, Energy Environ. Sci. 11 (2018) 772–799, https://doi.org/10.1039/C7EE03031B.

[26] M. Yu, J. Li, L. Wang, KOH-activated carbon aerogels derived from sodium carboxymethyl cellulose for high-performance supercapacitors and dye adsorption, Chem. Eng. J. 310 (2017) 300–306, https://doi.org/10.1016/j.cej.2016.10.121.

[27] S.H. Kwon, E. Lee, B.-S. Kim, S.-G. Kim, B.-J. Lee, M.-S. Kim, J.C. Jung, Preparation of activated carbon aerogel and its application to electrode material for electric double layer capacitor in organic electrolyte: effect of activation temperature, Korean J. Chem. Eng. 32 (2015) 248–254, https://doi.org/10.1007/s11814-014-0215-z.

[28] P. Hao, Z. Zhao, J. Tian, H. Li, Y. Sang, G. Yu, H. Cai, H. Liu, C.P. Wong, A. Umar, Hierarchical porous carbon aerogel derived from bagasse for high performance supercapacitor electrode, Nanoscale 6 (2014) 12120–12129, https://doi.org/10.1039/C4NR03574G.
[29] J.-H. Lee, S.-J. Park, Recent advances in preparations and applications of carbon aerogels: a review, Carbon 163 (2020) 1–18, https://doi.org/10.1016/j.carbon.2020.02.073.
[30] Y. Zhang, L. Gong, X. Xu, L. Zhao, K. Li, G. Liang, L. Li, Q. Xie, Synthesis of carbon aerogels with controlled morphology and pore structure to modulate their bulk density and thermal conductivity *via* a quick one-pot preparation strategy, Carbon 216 (2024) 118487, https://doi.org/10.1016/j.carbon.2023.118487.
[31] C. Yuan, D. Wang, Y. Zhang, K. Li, J. Ding, Research progress on preparation, modification, and application of phenolic aerogel, Nanotechnol. Rev. 12 (2023) 20230109, https://doi.org/10.1515/ntrev-2023-0109.
[32] J.R. Gissinger, S.R. Zavada, J.G. Smith, J. Kemppainen, I. Gallegos, G.M. Odegard, E.J. Siochi, K.E. Wise, Predicting char yield of high-temperature resins, Carbon 202 (2023) 336–347, https://doi.org/10.1016/j.carbon.2022.11.002.
[33] Y. Tang, G. Xu, S. Liu, M. Li, J. He, X. Wen, Activated carbon microspheres with high surface area for efficient organic contaminants removal, Colloids Surf. A Physicochem. Eng. Asp. 669 (2023) 131479, https://doi.org/10.1016/j.colsurfa.2023.131479.
[34] K. Li, W. Chen, H. Yang, Y. Chen, S. Xia, M. Xia, X. Tu, H. Chen, Mechanism of biomass activation and ammonia modification for nitrogen-doped porous carbon materials, Bioresour. Technol. 280 (2019) 260–268, https://doi.org/10.1016/j.biortech.2019.02.039.
[35] K.S.W. Sing, Reporting physisorption data for gas/solid systems with special reference to the determination of surface area and porosity (Recommendations 1984), Pure Appl. Chem. 57 (1985) 603–619, https://doi.org/10.1351/pac198557040603.
[36] D. Yan, L. Liu, X. Wang, K. Xu, J. Zhong, Biomass-derived activated carbon nanoarchitectonics with hibiscus flowers for high-performance supercapacitor electrode applications, Chem. Eng. Technol. 45 (2022) 649–657, https://doi.org/10.1002/ceat.202100585.
[37] X. Tian, S. Luo, R. Huang, M. Sun, Z. Zhang, S. Yan, Constructing hybrid nitrogen/oxygen-rich surface and hierarchically porous in lignite-based activated carbons as supercapacitor electrode by in-situ soda ash activate strategy, J. Alloys Compd. 1005 (2024) 176090, https://doi.org/10.1016/j.jallcom.2024.176090.
[38] Y.-J. Zhang, Z.-J. Xing, Z.-K. Duan, Meng Li, Y. Wang, Effects of steam activation on the pore structure and surface chemistry of activated carbon derived from bamboo waste, Appl. Surf. Sci. 315 (2014) 279–286, https://doi.org/10.1016/j.apsusc.2014.07.126.
[39] R. Tikoria, A. Kaur, P. Ohri, Physiological, biochemical and structural changes in tomato plants by vermicompost application in different exposure periods under glass house conditions, Plant Physiol. Biochem. 197 (2023) 107656, https://doi.org/10.1016/j.plaphy.2023.107656.
[40] A. Ariharan, K. Ramesh, R. Vinayagamoorthi, M.S. Rani, B. Viswanathan, S. Ramaprabhu, V. Nandhakumar, Biomass derived phosphorous containing porous carbon material for hydrogen storage and high-performance supercapacitor applications, J. Energy Storage 35 (2021) 102185, https://doi.org/10.1016/j.est.2020.102185.
[41] Y. Zhai, Y. Dou, D. Zhao, P.F. Fulvio, R.T. Mayes, S. Dai, Carbon materials for chemical capacitive energy storage, Adv. Mater. 23 (2011) 4828–4850, https://doi.org/10.1002/adma.201100984.
[42] R. Guo, C. Lv, W. Xu, J. Sun, Y. Zhu, X. Yang, J. Li, J. Sun, L. Zhang, D. Yang, Effect of intrinsic defects of carbon materials on the sodium storage performance, Adv. Energy Mater. 10 (2020) 1903652, https://doi.org/10.1002/aenm.201903652.
[43] Y. Ma, X. Meng, K. Li, L. Zhang, Y. Du, X. Cai, J. Qiu, Scrutinizing synergy and active site of nitrogen and selenium dual-doped porous carbon for efficient triiodide reduction, ACS Catal. 13 (2023) 1290–1298, https://doi.org/10.1021/acscatal.2c05024.
[44] B. Pollack, S. Holmberg, D. George, I. Tran, M. Madou, M. Ghazinejad, Nitrogen-rich polyacrylonitrile-based graphitic carbons for hydrogen peroxide sensing, Sensors 17 (2017) 2407, https://doi.org/10.3390/s17102407.
[45] V. Thapliyal, M.E. Alabdulkarim, D.R. Whelan, B. Mainali, J.L. Maxwell, A concise review of the Raman spectra of carbon allotropes, Diam. Relat. Mater. 127 (2022) 109180, https://doi.org/10.1016/j.diamond.2022.109180.
[46] V.V. Chesnokov, I.P. Prosvirin, E.Y. Gerasimov, A.S. Miliushina, The influence of carbon nanomaterials on catalytic decomposition of formic acid, Int. J. Hydrog. Energy 57 (2024) 530–539, https://doi.org/10.1016/j.ijhydene.2023.12.299.
[47] H.M. Morales, H. Vieyra, D.A. Sanchez, E.M. Fletes, M. Odlyzko, T.P. Lodge, V. Padilla-Gainza, M. Alcoutlabi, J.G. Parsons, Synthesis and characterization of titanium nitride–carbon composites and their use in lithium-ion batteries, Nanomaterials 14 (2024) 624, https://doi.org/10.3390/nano14070624.
[48] M. Lesňák, D. Cvejn, M. Petr, P. Peikertová, R. Gabor, T. Fördös, P. Czernek, D. Plachá, A novel N-doped carbon nanomaterial – carbon nano-mousse, J. Mater. Chem. A 11 (2023) 4627–4638, https://doi.org/10.1039/D2TA07947J.
[49] J. Wang, H. Liu, J. Diao, X. Gu, H. Wang, J. Rong, B. Zong, D.S. Su, Size-controlled nitrogen-containing mesoporous carbon nanospheres by one-step aqueous self-assembly strategy, J. Mater. Chem. A 3 (2015) 2305–2313, https://doi.org/10.1039/C4TA05820H.
[50] Z. Zhai, H. Li, Y. Zheng, Y. Ji, H. Peng, Y. Gao, M. Yan, H. Yu, High specific surface area carbon aerogel derived from starch for methylene blue adsorption and supercapacitors, Int. J. Biol. Macromol. 274 (2024) 133282, https://doi.org/10.1016/j.ijbiomac.2024.133282.
[51] Y.A. Haj, A.B. Soliman, J. Vapaavuori, M. Elbahri, Carbon aerogels derived from anion-modified nanocellulose for adaptive supercapacitor performance, Adv. Funct. Mater. 34 (2024) 2313117, https://doi.org/10.1002/adfm.202313117.
[52] C. Ding, X. Wang, P. Huang, J. Yu, Nitrogen-doped carbon aerogels derived from polyimide for high-performance supercapacitor, J. Mater. Sci. 57 (2022) 21680–21692, https://doi.org/10.1007/s10853-022-07986-z.
[53] L. Wang, Q. Wu, B. Zhao, Z. Li, Y. Zhang, L. Huang, S. Yu, Multi-functionalized carbon aerogels derived from chitosan, J. Colloid Interface Sci. 605 (2022) 790–802, https://doi.org/10.1016/j.jcis.2021.07.132.
[54] F. Shi, C. Chen, J. Liu, T. Yu, X. Wang, Construction of activated-CNT/carbon composite aerogel for supercapacitor electrode with ultra high cycle stability, J. Solid State Chem. 330 (2024) 124492, https://doi.org/10.1016/j.jssc.2023.124492.
[55] A.A. Edathil, B. Rezaei, K. Almdal, S.S. Keller, In situ mineralization of biomass-derived hydrogels boosts capacitive electrochemical energy storage in free-standing 3D carbon aerogels, Energy Environ. Mater. 7 (2024) e12591, https://doi.org/10.1002/eem2.12591.
[56] Z. Zhai, S. Wang, Y. Xu, L. Zhang, X. Wang, H. Yu, B. Ren, Starch-based carbon aerogels prepared by an innovative KOH activation method for supercapacitors, Int. J. Biol. Macromol. 257 (2024) 128587, https://doi.org/10.1016/j.ijbiomac.2023.128587.
[57] R.B. Marichi, S. Goel, A.K. Tomar, V. Sahu, S. Lalwani, G. Singh, R.K. Sharma, Direct hydrothermal treatment of sugarcane juice for 3D oxygen-rich carbon aerogel/$NiCo_2O_4$ based supercapacitor, Mater. Chem. Phys. 239 (2020) 121957, https://doi.org/10.1016/j.matchemphys.2019.121957.
[58] J. Xu, X. Zhou, M. Chen, S. Shi, Y. Cao, Preparing hierarchical porous carbon aerogels based on enzymatic hydrolysis lignin through ambient drying for supercapacitor electrodes, Microporous Mesoporous Mater. 265 (2018) 258–265, https://doi.org/10.1016/j.micromeso.2018.02.024.
[59] M. Oschatz, S. Boukhalfa, W. Nickel, J.P. Hofmann, C. Fischer, G. Yushin, S. Kaskel, Carbide-derived carbon aerogels with tunable pore structure as versatile electrode material in high power supercapacitors, Carbon 113 (2017) 283–291, https://doi.org/10.1016/j.carbon.2016.11.050.
[60] P. Hao, G. Cui, X. Shi, J. Xie, X. Xia, Y. Sang, C.P. Wong, H. Liu, B. Tang, High perfor- mance supercapacitors from hierarchical porous carbon aerogels based on sliced bread, Chin. J. Chem. 35 (2017) 699–706, https://doi.org/10.1002/cjoc.201600722.
[61] X. Yang, G. Sun, F. Wang, X. Li, Z. Zhang, Y. Zhen, D. Wang, X. Gao, F. Fu, R. Chi, Rational design of dense microporous carbon derived from coal tar pitch towards high mass loading supercapacitors, J. Colloid Interface Sci. 646 (2023) 228–237, https://doi.org/10.1016/j.jcis.2023.04.179.
[62] L. Ji, Y. Zhang, X. Li, T. Jiao, X. Dong, R. Zhang, P. Liang, Coral-like interconnected porous carbon derived from phenolic resin/ammonium alginate composite for high-rate supercapacitor, J. Power Sources 573 (2023) 232933, https://doi.org/10.1016/j.jpowsour.2023.232933.
[63] H.D. Asfaw, A. Kucernak, E.S. Greenhalgh, M.S.P. Shaffer, Electrochemical performance of supercapacitor electrodes based on carbon aerogel-reinforced spread tow carbon fiber fabrics, Compos. Sci. Technol. 238 (2023) 110042, https://doi.org/10.1016/j.compscitech.2023.110042.
[64] J. Li, Q. Lin, Z. Wang, A. Du, H. Luo, Y.-Q. Liu, Hierarchical porous carbon with high specific surface area and superb capacitance made from palm shells for supercapacitors, Diam. Relat. Mater. 135 (2023) 109852, https://doi.org/10.1016/j.diamond.2023.109852.
[65] T.B. Nguyen, B. Yoon, T.D. Nguyen, E. Oh, Y. Ma, M. Wang, J. Suhr, A facile salt-templating synthesis route of bamboo-derived hierarchical porous carbon for supercapacitor applications, Carbon 206 (2023) 383–391, https://doi.org/10.1016/j.carbon.2023.02.060.
[66] M. Ma, J. Zhang, Y. Huan, M. Ren, T. Wei, S. Yan, 3D stack tubular mesoporous carbon derived from discarded sesame capsule shells for high-performance supercapacitors, Diam. Relat. Mater. 131 (2023) 109562, https://doi.org/10.1016/j.diamond.2022.109562.
[67] H. Lindström, S. Södergren, A. Solbrand, H. Rensmo, J. Hjelm, A. Hagfeldt, S.-E. Lindquist, Li^+ ion insertion in TiO_2 (anatase). 2. Voltammetry on nanoporous films, J. Phys. Chem. B 101 (1997) 7717–7722, https://doi.org/10.1021/jp970490q.
[68] S. Seenivasan, K.I. Shim, C. Lim, T. Kavinkumar, A.T. Sivagurunathan, J.W. Han, D.-H. Kim, Boosting pseudocapacitive behavior of supercapattery electrodes by incorporating a schottky junction for ultrahigh energy density, Nano-Micro Lett. 15 (2023) 62, https://doi.org/10.1007/s40820-023-01016-6.
[69] K.A.S. Raj, K. Pramoda, C.S. Rout, Assembling a high-performance asymmetric supercapacitor based on pseudocapacitive S-doped VSe_2/CNT hybrid and 2D borocarbonitride nanosheets, J. Mater. Chem. C 11 (2023) 2565–2573, https://doi.org/10.1039/D2TC04600H.